

Experimental observation of spontaneous symmetry breaking in a quantum phase transition

Wen Ning,^{1,*} Ri-Hua Zheng,^{1,†} Jia-Hao Lü,¹ Fan Wu,¹ Zhen-Biao Yang,^{1,2,‡} and Shi-Biao Zheng^{1,2,§}

¹*Fujian Key Laboratory of Quantum Information and Quantum Optics,
College of Physics and Information Engineering,
Fuzhou University, Fuzhou, Fujian, 350108, China*
²*Hefei National Laboratory, Hefei 230088, China*

Spontaneous symmetry breaking (SSB) plays a central role in understanding a large variety of phenomena associated with phase transitions, such as superfluid and superconductivity. So far, the transition from a symmetric vacuum to a macroscopically ordered phase has been substantially explored. The process bridging these two distinct phases is critical to understanding how a classical world emerges from a quantum phase transition, but so far remains unexplored in experiment. We here report an experimental demonstration of such a process with a quantum Rabi model engineered with a superconducting circuit. We move the system from the normal phase to the superradiant phase featuring two symmetry-breaking field components, one of which is observed to emerge as the classical reality. The results demonstrate that the environment-induced decoherence plays a critical role in the SSB.

PACS numbers: 03.65.Ud, 03.67.-a, 42.50.Pq

Keywords: quantum phase transition, Rabi model, spontaneous symmetry breaking, superconducting circuit, Schrödinger cat states

I. INTRODUCTION

The concept of spontaneous symmetry breaking (SSB) has infiltrated almost all research branches of modern physics, ranging from condensed physics [1] to quantum field theory [2, 3]. SSB appears when the observed systems lack the symmetry of the governing physical laws. It underlies phase transitions described by the Ginzburg-Landau-Wilson paradigm, e.g., Bardeen-Cooper-Schrieffer superconducting phenomena [4], and is critical to the Higgs mechanism [5], where the mass is generated by breaking the invariance associated with the Lagrangian. Besides these, SSB plays an important role in the evolution of biology, e.g., the visual cortex processes image by spontaneously breaking both the translation and rotation symmetries, which was recently interpreted in terms of zero-temperature phase transitions [6]. In a more general sense, SSB is responsible for the formation of the universe [7], and thus gives rise to the infinite diversity of nature.

In quantum field theory, SSB occurs in an infinitely extended system that possesses degenerate vacua. In this case, an infinitesimal perturbation is sufficient to single out one of these vacua as the real ground state. For a quantum system with a definite size, the symmetry is generally broken by the decoherence process [8–10], where the environment or a monitoring meter continuously gathers the information about the system by entangling its state with the system. This process progressively

destroys the quantum coherence between the symmetrically superposed quasiclassical components with broken symmetry, transforming the quantum superposition into a classical mixture [11]. The decoherence rate linearly scales with the size of the system, which prohibits observation of quantum superpositions in a macroscopic object, such as the famous Schrödinger cat [12]. In this case, the environment or meter plays a central role in the symmetry breaking of the observed system.

Despite impressive experimental demonstrations in classical systems [13–17], observations of the SSB associated with quantum phase transitions have remained an outstanding task. As the energy gap vanishes at the critical point, an adiabatic evolution across this point would require an infinitely long time. For this reason, experimental demonstrations of quantum phase transitions have been focused on out-of-equilibrium systems [18–34], where transitions between distinct phases were realized by a quenching process or in a dynamical manner. In thus-realized superradiant phase transitions (SPTs) with an ultracold atomic gas trapped in an optical cavity, the breaking of both discrete [30] and continuous translation symmetries [31, 32] have been observed. However, in these experiments, the symmetries were not broken spontaneously, but explicitly with a small symmetry-breaking field or by a detuning that broke the Hamiltonian symmetry. In two very recent experiments, continuous symmetry-breaking phases were prepared in a one-dimensional ionic chain [35] and a two-dimensional Rydberg array [36], respectively. Despite these impressive progresses, it remains an experimental challenge to directly observe how the SSB occurs during a quantum phase transition, which is responsible for the emergence of a classical, symmetry-breaking state under a symmetric Hamiltonian.

* These authors equally contributed to the work.

† ruazheng@gmail.com; These authors equally contributed to the work.

‡ zbyang@fzu.edu.cn

§ fjqiqo@fzu.edu.cn

II. PHYSICAL MODEL AND THEORETICAL PREDICTIONS

We here report an experimental observation of such a process in an effective Rabi model, engineered in a circuit quantum electrodynamics (QED) architecture. With the high level of control over the effective coupling between the qubit and the photonic field involved in the Rabi Hamiltonian, we realize a second-order SPT, where the system is moved from a normal phase (NP) to a super-radiant phase (SP) formed by two coherent field states correlated to different qubit states. We observe the progressive evolution of the field from the initial symmetric vacuum to two superposed components, each of which has a broken symmetry in phase space, and the transition of their symmetric superposition to a classical mixture during their growth. Our results reveal that SSB is closely related to a quantum natural selection made by the environment [37], which continuously performs measurements on the system but with inaccessible records, washing the quantum coherence between the two quasi-classical components emerging from a quantum phase transition.

The system under investigation is comprised of a qubit and a photonic field, coupled by the Rabi Hamiltonian [38, 39]

$$H_{RM} = \delta a^\dagger a + \frac{1}{2}\Omega\sigma_z + \frac{1}{2}\lambda\sigma_x(a^\dagger + a). \quad (1)$$

Here a^\dagger and a denote the creation and annihilation operators for the photonic field with a frequency δ , $\sigma_x = |e\rangle\langle g| + |g\rangle\langle e|$ and $\sigma_z = |e\rangle\langle e| - |g\rangle\langle g|$ are pseudo-spin operators for the qubit, which has a frequency Ω , and whose upper and lower levels are denoted as $|e\rangle$ and $|g\rangle$. The qubit-resonator coupling strength is λ . The Rabi Hamiltonian is invariant under the parity transformation $(-1)^{a^\dagger a + |e\rangle\langle e|}$, featuring a Z_2 symmetry. In the limit $\Omega/\delta \rightarrow \infty$, the system has a unique ground state below the critical point $\xi = \lambda/\sqrt{\Omega\delta} = 1$, given by $|\psi_{np}\rangle = S(r_{np})|0\rangle|g\rangle$, where $S(r_{np})$ is a squeezing operator with $r_{np} = -\frac{1}{4}\ln(1 - \xi^2)$. Due to the limited frequency ratio Ω/δ in a real experiment, when $\xi < 1$, the field in the experimentally realized Rabi model almost remains in the vacuum state, which is significantly distinct from the ideal ground state for $\Omega/\delta \rightarrow \infty$. Above the critical point, the system enters the SP, characterized by two degenerate ground states $|\psi_{sp}^\pm\rangle = D(\pm\alpha)S(r_{sp})|0\rangle|\pm\rangle$, where $r_{sp} = -\frac{1}{4}\ln(1 - \xi^{-4})$, $D(\alpha) = \exp[\alpha(a^\dagger - a)]$ with $\alpha = \sqrt{\frac{\Omega}{4\xi^2\delta}(\xi^4 - 1)}$, and $|\pm\rangle$ are two qubit basis states. Compared with the case in the Dicke model, the SPT in the Rabi mode is realized by replacing thermodynamical limit with the scaling limit, where the frequency ratio between qubit and the field tends to infinity [39]. Each of these ground states is symmetry-broken, signified by the nonvanishing coherence $\langle\psi_{sp}^\pm|a|\psi_{sp}^\pm\rangle = \pm\alpha$ [39]. Under unitary Hamiltonian dynamics, adiabatically increasing the parameter ξ across the critical point would evolve

the system to the equal superposition of the two degenerate ground states

$$|\psi_e\rangle = N_e(|\psi_{sp}^+\rangle + |\psi_{sp}^-\rangle), \quad (2)$$

which preserves the parity of the ground state below the critical point. However, during the evolution, the system is inevitably coupled to the environment, which continuously monitors the system in the preferred basis [11], forcing the system to choose between these two conflicting classical states.

III. DEVICE AND EXPERIMENTAL SCHEME

The experiment is performed with a circuit QED device, which involves a resonator of a fixed frequency $\omega_r/2\pi = 5.581$ GHz controllably coupled to 5 frequency-tunable Xmon qubits, with an on-resonance coupling strength of $g/2\pi \simeq 20$ MHz. One of these qubits is used as the test qubit for realizing the Rabi model, while the other qubits are effectively decoupled from the resonator during the quenching process due to the large detunings. The experiment starts by tuning the test qubit to the frequency $\omega_q/2\pi = 5.21$ GHz, where it is subjected to a transverse microwave driving of an amplitude $A = 2\pi \times 15$ MHz and two longitudinal parametric modulations, one having a fixed frequency $\nu_1/2\pi = 185$ MHz and amplitude $\varepsilon_1 = 2\pi \times 146$ MHz, while the other bearing a fixed frequency $\nu_2/2\pi = 25.97$ MHz but a tunable amplitude ε_2 . With this setting, the qubit is coupled to the transverse field at the carrier and to the resonator at the second upper sideband with respect to the first modulation [22]. In the framework coinciding with the Rabi precession associated with the transverse drive and discarding the fast rotating terms, the system dynamics can be described by the effective Rabi Hamiltonian with an effective coupling strength $\lambda = gJ_2(\mu)/2 = 2\pi \times 0.735$ MHz, where $J_n(\mu)$ is the n th Bessel function of the first kind with $\mu = \varepsilon_1/\nu_1$. The effective qubit frequency and resonator frequency are $\Omega = \varepsilon_2/2$ and $\delta = \omega_r - \omega_q - 2\nu_1$, respectively. The quench parameter ξ is controllable by adjusting the amplitude ε_2 of the second parametric modulation and by tuning the Stark shift of the resonator produced by an ancilla qubit dispersively coupled to the resonator.

The quench parameter ξ is modeled as a linear function of time, $\xi = 0.5 + 2t/(3 \mu s)$. We first investigate the evolution of the resonator irrespective of the qubit state. To monitor the real-time evolution of the resonator, after a preset quench time t we switch off both the transverse and longitudinal drives, decoupling the test qubit from the resonator. Then the Wigner tomography of the resonator's state is performed by applying a microwave pulse to the resonator to produce a displacement operation $D(-\beta)$, tuning an ancilla qubit on resonance with the resonator for a given time, and then biasing it back to its idle frequency for state readout. The Wigner function and the reduced density operator ρ_r for the resonator can

be extracted from the recorded Rabi oscillations signals of the ancilla qubit.

IV. LOSS-INDUCED SSB

The classical characteristic of the field can be well characterized by the Q-function, defined as, $Q(\gamma) = \frac{1}{\pi} \langle \gamma | \rho_r | \gamma \rangle$, where $|\gamma\rangle$ is the coherent state with a complex amplitude γ . The resonator's Q-functions, measured for quench times $t = 0, 2.0, 2.5,$ and $2.8 \mu\text{s}$, are displayed in Fig. 1a. As expected, the Q function gradually evolves from the single- to double-peak structure during the quenching process. Each of these two peaks corresponds to a quasi-classical state with a broken symmetry, manifested by the nonzero phase-space coordinates of the local maxima, α_+ and α_- , which can serve as the order parameter [40]. The two peaks correspond to quasi-classical coherent states $|\pm\alpha\rangle$ with complex amplitudes $\pm\alpha$. The two-peak pattern represents a signature of the second-order phase transition without coexistence of the normal and superradiant phases. This phase transition is in distinct contrast with the first-order SPT that features emergence of three peaks [41], one of which corresponds to the NP that coexists with the two SP components, as demonstrated in the previous experiment [22]. This significant distinction is mainly due to the fact that the control parameter ξ is linearly increased in the present experiment, but scaled in a highly nonlinear manner in the previous experiment. Due to the limitation of the experimental frequency ratio, $\Omega/\delta = 10$, the photon number does not show a divergent behavior at the critical point $\xi = 1$, corresponding to $t = 0.75 \mu\text{s}$, as shown in Fig. S3. This is due to the fact that the strongly squeezed resonator state, predicted to emerge near the critical point for the infinite frequency ratio [39], does not appear in the experiment.

Figure. 1b displays the measured $|\alpha_+|$ (dots) and $|\alpha_-|$ (triangles) versus time. Due to the experimental imperfections, there is a certain degree of unbalance between the two degenerate ground states, which is continually enlarged when the control parameter ξ is increased. This discrepancy manifests the explicit symmetry breaking owing to the deviation of the realized Hamiltonian dynamics from the ideal symmetric case, which, however, does not destroy the quantum coherence between the two superimposing ground states. We here focus on the SSB process where one of the two growing coherent states is singled out as the classical reality by the environment, which continuously gathers the information about which classical state the system is in, thereby deteriorating the quantum coherence that makes the two classical states suspending. The Q-functions of the resonator do not manifest the quantum coherence between the classical components. To obtain full information about this non-classical behavior, it is necessary to perform a joint qubit-resonator state tomography. The information of the field state associated with the qubit state $|j\rangle$ ($j = g, e$) is con-

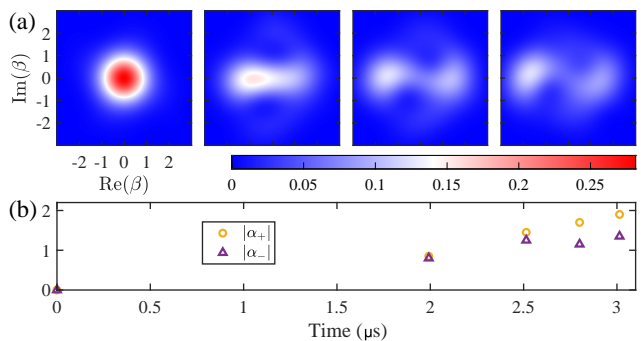


FIG. 1. **Observation of phase-space evolution during the SPT.** (a) Q-functions, measured for quench times $t = 0, 2.0, 2.5,$ and $2.8 \mu\text{s}$. During the process, the quench parameter as a function of time is modeled as $\xi = 0.5 + 2t/(3 \mu\text{s})$. After the interaction between the test qubit and the resonator is effectively switched off, the resonator state is read out by subsequently performing a phase-space translation to the resonator, resonantly coupling it to an ancilla qubit, and recording the Rabi signals of the ancilla. (b) Phase-space coordinates of the local maxima, α_+ and α_- , versus quench time.

tained in the corresponding Wigner function, defined as

$$\mathcal{W}_j(\beta) = \frac{2}{\pi P_j} \sum (-1)^n P_{j,n}(\beta), \quad (3)$$

where $P_{j,n}(\beta) = \langle j, n | D(-\beta) \rho D(\beta) | j, n \rangle$, and P_j is the probability of detecting the qubit in $|j\rangle$ -state. Here the symbol “ n ” denotes the photon number in the resonator. These matrix elements are extracted by detecting the test qubit, and correlating the measurement outcome to the Rabi oscillation signals of the ancilla qubit resonantly coupled to the resonator following a displacement operation $D(-\beta)$ [22, 42, 43]. Figure. 2a shows the conditional Wigner function, $\mathcal{W}_e(\beta)$, measured after quench times $t = 2.5, 2.8,$ and $3.0 \mu\text{s}$. The results clearly reveal a progressive loss of the quantum coherence between the two classical components, manifested by the gradual washing-out of the interference fringes between the two Gaussian-like peaks. Such a process can be understood in terms of the competition between the symmetric Hamiltonian dynamics and naturally-occurring dissipation, which continuously leaks the phase information about the growing field to the environment [10, 11]. This natural information acquisition accounts for coherence loss between the two suspending classical states, which leads to the SSB during the quantum phase transition. Due to the imperfect Hamiltonian control, the two Gaussian peaks are gradually diffused during the quench, which limits the size of the accessible output coherent field. The observation of the SSB can be pushed to a larger size with a more deliberately designed and fabricated device. The other conditional Wigner function $\mathcal{W}_g(\beta)$ measured exhibits a similar evolution behavior, as shown in Fig. 2b. In all the displayed Wigner functions, the main interference fringes appear in a region around the origin, which agrees with the numerical simulation presented in Fig.

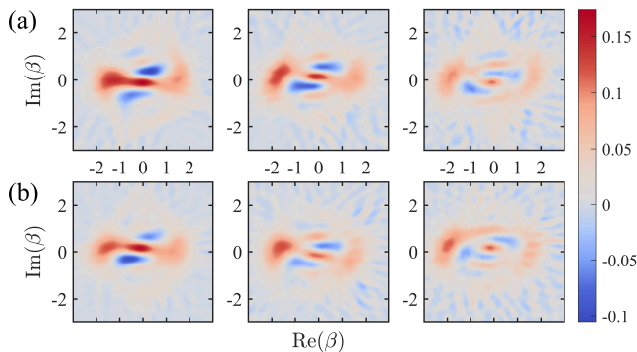


FIG. 2. **Observation of the loss of the quantum coherence.** (a) Wigner functions associated with the qubit state $|e\rangle$, measured after quench times $t = 2.5, 2.8,$ and $3.0 \mu\text{s}$. The results are obtained by correlating the Wigner function of the resonator to the measurement outcome $|e\rangle$ of the test qubit. (b) Measured Wigner functions associated with the qubit state $|g\rangle$.

S6. It should be noted that the measured Q functions and Wigner functions present symmetric structures even for a classical mixture, which can be interpreted as follows. For each experimental implementation, one of the two symmetry-breaking classical states, but not both, is singled out as the reality. The symmetry of the phase-space distribution associated with such a classical mixture reflects that the two conflicting classical realities appear with the same probability.

Previously, the decoherence processes of Schrödinger-cat-like quantum superpositions have been demonstrated in cavity QED [44, 45], ion-trap [46] and mechanical resonators [47], where the cat states were pre-prepared, following which the decoherence effects were observed. However, in reality, the environment is always playing its role, instead of waiting to set in until the cat state has grown up. Our experiment illustrates such a process, where the parity symmetry is broken as a consequence of the competition between the unitary breeding of the cat state and the environment-induced dissipation. Such a competition is critical to the emergence of the classical reality from a quantum world, but has not been experimentally reported so far. Our results reveal that decoherence is responsible for breaking the symmetry inherent in the Hamiltonian dynamics.

The symmetry-breaking process can be further characterized by the evolution of the nonclassical volume [48], defined as the phase-space integral of the quasi-probability distribution over the regions with negative values. The nonclassical volume of the field state associated with the qubit state $|j\rangle$ is calculated as $\mathcal{V}_k = (1 - \int d^2 \beta |\mathcal{W}_k(\beta)|) / 2$ which quantifies the quantum coherence between the two classical components. Figure. 3 displays \mathcal{V}_e and \mathcal{V}_g , inferred from the Wigner matrices reconstructed for different quench times. When the phase-space separation between $|\alpha_{\pm}\rangle$ is small, the unitary dynamics dominate over the environment-induced

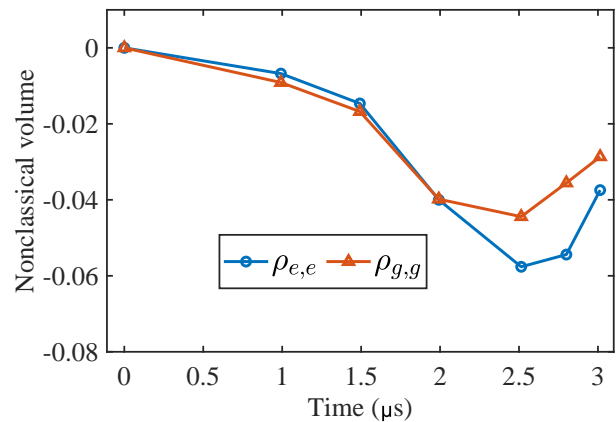


FIG. 3. **Measured nonclassical volumes (\mathcal{V}_k) for different the quench time.** The nonclassical volume of the resonator's output state associated with the qubit state $|k\rangle$ ($k = e, g$) is defined as the integral of the corresponding Wigner function $\mathcal{W}_k(\beta)$ over the regions in phase space where $\mathcal{W}_k(\beta)$ is negative. As the negativity is a consequence of the phase-space quantum interference between the two classical components, the evolution of \mathcal{V}_k manifests the process during which how the quantum coherence grows and then drops under the competition between the Hamiltonian dynamics and decoherence.

decoherence, so that the quantum coherence is improved with the quench time. With the growth of the photon number, the cat state becomes increasingly vulnerable to decoherence. Finally, decoherence plays a dominant role, destroying the quantum coherence between the two classical components, and manifesting SSB.

V. CONCLUSION

In conclusion, we have observed the spontaneous symmetry-breaking process in the second-order phase transition, realized with an effective Rabi model synthesized in a superconducting circuit. With a high level of control over the system parameters, we move the system from the NP to a SP with two symmetry-breaking classical components, each corresponding to a photonic coherent state with a well-defined amplitude and phase. We monitor the SSB process, during which one of these two components is singled out as the classical reality. The results build a close relationship between SSB and environment-induced decoherence. With the improvement of the coherence times of the system, a SSB process can be observed with a larger cat size, which would shed new light on the quantum-to-classical transition.

VI. ACKNOWLEDGEMENTS

Funding: This work was supported by the National Natural Science Foundation of China under (Grant No.

11874114, Grants No. 12274080, and No. 11875108) and Innovation Program for Quantum Science and Technology under Grant No. 2021ZD0300200. **Competing interests:** The authors declare that they have no competing interests. **Data and materials availability:** All

data needed to evaluate the conclusions in the paper are present in the paper and/or the Supplementary Materials. Additional data related to this paper may be requested from the authors.

-
- [1] S. Sachdev, *Quantum Phase Transitions*, 2nd ed. (Cambridge University Press, 2011).
- [2] Y. Nambu, Nobel lecture: Spontaneous symmetry breaking in particle physics: A case of cross fertilization, *Rev. Mod. Phys.* **81**, 1015 (2009).
- [3] S. Weinberg, The making of the standard model, *Eur. Phys. J. C* **34**, 5 (2004).
- [4] J. Bardeen, L. N. Cooper, and J. R. Schrieffer, Theory of superconductivity, *Phys. Rev.* **108**, 1175 (1957).
- [5] J. Bernstein, Spontaneous symmetry breaking, gauge theories, the Higgs mechanism and all that, *Rev. Mod. Phys.* **46**, 7 (1974).
- [6] F. Fumarola, B. Hein, and K. D. Miller, Mechanisms for spontaneous symmetry breaking in developing visual cortex, *Phys. Rev. X* **12**, 031024 (2022).
- [7] T. Kibble, Some implications of a cosmological phase transition, *Phys. Rep.* **67**, 183 (1980).
- [8] J. van Wezel, J. van den Brink, and J. Zaanen, An intrinsic limit to quantum coherence due to spontaneous symmetry breaking, *Phys. Rev. Lett.* **94**, 230401 (2005).
- [9] J. Dziarmaga, W. H. Zurek, and M. Zwolak, Non-local quantum superpositions of topological defects, *Nat. Phys.* **8**, 49 (2012).
- [10] L. P. García-Pintos, D. Tielas, and A. del Campo, Spontaneous symmetry breaking induced by quantum monitoring, *Phys. Rev. Lett.* **123**, 090403 (2019).
- [11] W. H. Zurek, Decoherence and the transition from quantum to classical, *Phys Today* **44**, 36 (1991).
- [12] E. Schrödinger, Die gegenwärtige situation in der quantenmechanik, *Die Naturwissenschaften* **23**, 807 (1935).
- [13] M. Liu, D. A. Powell, I. V. Shadrivov, M. Lapine, and Y. S. Kivshar, Spontaneous chiral symmetry breaking in metamaterials, *Nat. Commun* **5**, 4441 (2014).
- [14] P. Hamel, S. Haddadi, F. Raineri, P. Monnier, G. Beaudoin, I. Sagnes, A. Levenson, and A. M. Yacomotti, Spontaneous mirror-symmetry breaking in coupled photonic-crystal nanolasers, *Nat. Photonics* **9**, 311 (2015).
- [15] Q.-T. Cao, H. Wang, C.-H. Dong, H. Jing, R.-S. Liu, X. Chen, L. Ge, Q. Gong, and Y.-F. Xiao, Experimental demonstration of spontaneous chirality in a nonlinear microresonator, *Phys. Rev. Lett.* **118**, 033901 (2017).
- [16] G. Xu, A. U. Nielsen, B. Garbin, L. Hill, G.-L. Oppo, J. Fatome, S. G. Murdoch, S. Coen, and M. Erkintalo, Spontaneous symmetry breaking of dissipative optical solitons in a two-component Kerr resonator, *Nat. Commun* **12**, 4023 (2021).
- [17] B. Garbin, A. Giraldo, K. J. H. Peters, N. G. R. Broderick, A. Spakman, F. Raineri, A. Levenson, S. R. K. Rodriguez, B. Krauskopf, and A. M. Yacomotti, Spontaneous symmetry breaking in a coherently driven nanophotonic Bose-Hubbard dimer, *Phys. Rev. Lett.* **128**, 053901 (2022).
- [18] M.-L. Cai, Z.-D. Liu, W.-D. Zhao, Y.-K. Wu, Q.-X. Mei, Y. Jiang, L. He, X. Zhang, Z.-C. Zhou, and L.-M. Duan, Observation of a quantum phase transition in the quantum Rabi model with a single trapped ion, *Nat. Commun.* **12**, 1126 (2021).
- [19] A. Safavi-Naini, R. J. Lewis-Swan, J. G. Bohnet, M. Gärtner, K. A. Gilmore, J. E. Jordan, J. Cohn, J. K. Freericks, A. M. Rey, and J. J. Bollinger, Verification of a many-ion simulator of the Dicke model through slow quenches across a phase transition, *Phys. Rev. Lett.* **121**, 040503 (2018).
- [20] M. Feng, Y. Zhong, T. Liu, L. Yan, W. Yang, J. Twamley, and H. Wang, Exploring the quantum critical behaviour in a driven Tavis-Cummings circuit, *Nat. Commun.* **6**, 7111 (2015).
- [21] J. M. Fink, A. Dombi, A. Vukics, A. Wallraff, and P. Domokos, Observation of the photon-blockade breakdown phase transition, *Phys. Rev. X* **7**, 011012 (2017).
- [22] R.-H. Zheng, W. Ning, Y.-H. Chen, J.-H. Lü, L.-T. Shen, K. Xu, Y.-R. Zhang, D. Xu, H. Li, Y. Xia, F. Wu, Z.-B. Yang, A. Miranowicz, N. Lambert, D. Zheng, H. Fan, F. Nori, and S.-B. Zheng, Observation of a superradiant phase transition with emergent cat states, *Phys. Rev. Lett.* **131**, 113601 (2023).
- [23] J. Zhang, G. Pagano, P. W. Hess, A. Kyprianidis, P. Becker, H. Kaplan, A. V. Gorshkov, Z.-X. Gong, and C. Monroe, Observation of a many-body dynamical phase transition with a 53-qubit quantum simulator, *Nature* **551**, 601 (2017).
- [24] P. Jurcevic, H. Shen, P. Hauke, C. Maier, T. Brydges, C. Hempel, B. P. Lanyon, M. Heyl, R. Blatt, and C. F. Roos, Direct observation of dynamical quantum phase transitions in an interacting many-body system, *Phys. Rev. Lett.* **119**, 080501 (2017).
- [25] K. Xu, Z.-H. Sun, W. Liu, Y.-R. Zhang, H. Li, H. Dong, W. Ren, P. Zhang, F. Nori, D. Zheng, H. Fan, and H. Wang, Probing dynamical phase transitions with a superconducting quantum simulator, *Sci. Adv.* **6**, eaba4935 (2020).
- [26] J. Klinder, H. Keßler, M. Wolke, L. Mathey, and A. Hemmerich, Dynamical phase transition in the open Dicke model, *Proc. Natl. Acad. Sci. U.S.A.* **112**, 3290 (2015).
- [27] Z. Zhiqiang, C. H. Lee, R. Kumar, K. J. Arnold, S. J. Masson, A. S. Parkins, and M. D. Barrett, Nonequilibrium phase transition in a spin-1 Dicke model, *Optica* **4**, 424 (2017).
- [28] K. Baumann, C. Guerlin, F. Brennecke, and T. Esslinger, Dicke quantum phase transition with a superfluid gas in an optical cavity, *Nature* **464**, 1301 (2010).
- [29] F. Brennecke, R. Mottl, K. Baumann, R. Landig, T. Donner, and T. Esslinger, Real-time observation of fluctuations at the driven-dissipative Dicke phase transition, *Proc. Natl. Acad. Sci. U.S.A.* **110**, 11763 (2013).
- [30] K. Baumann, R. Mottl, F. Brennecke, and T. Esslinger, Exploring symmetry breaking at the Dicke quantum phase transition, *Phys. Rev. Lett.* **107**, 140402 (2011).

- [31] J. Léonard, A. Morales, P. Zupancic, T. Esslinger, and T. Donner, Supersolid formation in a quantum gas breaking a continuous translational symmetry, *Nature* **543**, 87 (2017).
- [32] J. Léonard, A. Morales, P. Zupancic, T. Donner, and T. Esslinger, Monitoring and manipulating Higgs and Goldstone modes in a supersolid quantum gas, *Science* **358**, 1415 (2017).
- [33] F. Ferri, R. Rosa-Medina, F. Finger, N. Dogra, M. Soriante, O. Zilberberg, T. Donner, and T. Esslinger, Emerging dissipative phases in a superradiant quantum gas with tunable decay, *Phys. Rev. X* **11**, 041046 (2021).
- [34] X. Zhang, Y. Chen, Z. Wu, J. Wang, J. Fan, S. Deng, and H. Wu, Observation of a superradiant quantum phase transition in an intracavity degenerate Fermi gas, *Science* **373**, 1359 (2021).
- [35] L. Feng, O. Katz, C. Haack, M. Maghrebi, A. V. Gorshkov, Z. Gong, M. Cetina, and C. Monroe, *Continuous symmetry breaking in a trapped-ion spin chain* (2022), arXiv:2211.01275 [cond-mat, physics:quant-ph].
- [36] C. Chen, G. Bornet, M. Bintz, G. Emperauger, L. Leclerc, V. S. Liu, P. Scholl, D. Barredo, J. Hauschild, S. Chatterjee, M. Schuler, A. M. Läuchli, M. P. Zaletel, T. Lahaye, N. Y. Yao, and A. Browaeys, Continuous symmetry breaking in a two-dimensional Rydberg array, *Nature* **616**, 691 (2023).
- [37] S. Lloyd, A quantum of natural selection, *Nat. Phys.* **5**, 164 (2009).
- [38] S. Ashhab, Superradiance transition in a system with a single qubit and a single oscillator, *Phys. Rev. A* **87**, 013826 (2013).
- [39] M.-J. Hwang, R. Puebla, and M. B. Plenio, Quantum phase transition and universal dynamics in the Rabi model, *Phys. Rev. Lett.* **115**, 180404 (2015).
- [40] M.-J. Hwang and M. B. Plenio, Quantum phase transition in the finite Jaynes-Cummings lattice systems, *Phys. Rev. Lett.* **117**, 123602 (2016).
- [41] C. J. Zhu, L. L. Ping, Y. P. Yang, and G. S. Agarwal, Squeezed light induced symmetry breaking superradiant phase transition, *Phys. Rev. Lett.* **124**, 073602 (2020).
- [42] M. Hofheinz, H. Wang, M. Ansmann, R. C. Bialczak, E. Lucero, M. Neeley, A. D. O’Connell, D. Sank, J. Wenner, J. M. Martinis, and A. N. Cleland, Synthesizing arbitrary quantum states in a superconducting resonator, *Nature* **459**, 546 (2009).
- [43] S.-B. Zheng, Y.-P. Zhong, K. Xu, Q.-J. Wang, H. Wang, L.-T. Shen, C.-P. Yang, J. M. Martinis, A. N. Cleland, and S.-Y. Han, Quantum delayed-choice experiment with a beam splitter in a quantum superposition, *Phys. Rev. Lett.* **115**, 260403 (2015).
- [44] M. Brune, E. Hagley, J. Dreyer, X. Maître, A. Maali, C. Wunderlich, J. M. Raimond, and S. Haroche, Observing the progressive decoherence of the “meter” in a quantum measurement, *Phys. Rev. Lett.* **77**, 4887 (1996).
- [45] S. Deléglise, I. Dotsenko, C. Sayrin, J. Bernu, M. Brune, J.-M. Raimond, and S. Haroche, Reconstruction of non-classical cavity field states with snapshots of their decoherence, *Nature* **455**, 510 (2008).
- [46] C. J. Myatt, B. E. King, Q. A. Turchette, C. A. Sackett, D. Kielpinski, W. M. Itano, C. Monroe, and D. J. Wineland, Decoherence of quantum superpositions through coupling to engineered reservoirs, *Nature* **403**, 269 (2000).
- [47] M. Bild, M. Fadel, Y. Yang, U. von Lüpke, P. Martin, A. Bruno, and Y. Chu, Schrödinger cat states of a 16-microgram mechanical oscillator, *Science* **380**, 274 (2023).
- [48] A. Kenfack and K. Życzkowski, Negativity of the wigner function as an indicator of non-classicality, *J. Opt. B: Quantum Semiclass. Opt.* **6**, 396 (2004).

Supplementary Material for “Experimental observation of spontaneous symmetry breaking in a quantum phase transition”

Wen Ning,^{1,*} Ri-Hua Zheng,^{1,†} Jia-Hao Lü,¹ Fan Wu,¹ Zhen-Biao Yang,^{1,2,‡} and Shi-Biao Zheng^{1,2,§}

¹*Fujian Key Laboratory of Quantum Information and Quantum Optics,
College of Physics and Information Engineering,
Fuzhou University, Fuzhou, Fujian, 350108, China*

²*Hefei National Laboratory, Hefei 230088, China*

(Dated: July 1, 2024)

CONTENTS

S1. Derivation of the effective Hamiltonian	1
S2. Control of the quenching dynamics	2
A. Time-dependence of the normalized coupling parameter ξ	2
B. Control of the effective qubit frequency Ω and the effective resonator frequency δ	2
C. Phase optimization of two longitudinal modulations	3
S3. Characterization of the resonator state	3
A. Measurement of photon-number distribution	3
B. Reconstruction of conditional Wigner functions	4
C. Correction of the phase-space rotations	6
S4. Numerical simulation	6
References	6

S1. DERIVATION OF THE EFFECTIVE HAMILTONIAN

The physical model considered is composed of a photonic field coupling to a qubit, whose frequency is modulated according to $\omega_q(t) = \omega_0 + \varepsilon_1 \cos(\nu_1 t) + \varepsilon_2 \cos(\nu_2 t)$. Besides, the qubit is transversely driven by an external field at the frequency ω_0 with an amplitude A , the Hamiltonian in the rotating frame with respect to $H_0 = (\omega_0 + 2\nu_1)a^\dagger a + [\omega_0 + \varepsilon_1 \cos(\nu_1 t)]\sigma_z/2$ is ($\hbar = 1$ hereafter)

$$H'_I = \delta a^\dagger a + \frac{1}{2}\varepsilon_2 \cos(\nu_2 t)\sigma_z + \left\{ \exp[-i\mu \sin(\nu_1 t)] [g \exp(2i\nu_1 t) a^\dagger + A] \sigma_- + \text{H.c.} \right\}. \quad (\text{S1})$$

Here, $\mu = \varepsilon_1/\nu_1$, δ is the effective resonator frequency, g is the qubit-resonator coupling strength measured on their resonance, ω_0 corresponds to the mean transition frequency of the qubit, and ε_j (ν_j) is the j th modulation amplitude (frequency). The above Hamiltonian can be expanded by the Jacobi-Anger expansion as

$$H'_I = \delta a^\dagger a + \frac{1}{2}\varepsilon_2 \cos(\nu_2 t)\sigma_z + \sum_{m=-\infty}^{\infty} H_m, \quad (\text{S2})$$

$$H_m = J_m(\mu) \left\{ g \exp[-i(m-2)\nu_1 t] a^\dagger + A \exp(-im\nu_1 t) \right\} \sigma_- + \text{H.c.}$$

* These authors equally contributed to the work.

† ruazheng@gmail.com; These authors equally contributed to the work.

‡ zbyang@fzu.edu.cn

§ fqiqo@fzu.edu.cn

Under the condition $\{|gJ_2(\mu)|, |AJ_0(\mu)|, \delta, \varepsilon_2\} \ll \nu_1$, the fast-oscillating terms can be discarded. In such a case, H'_I reduces to

$$\begin{aligned} H'_I &= \delta a^\dagger a + \frac{1}{2}\varepsilon_2 \cos(\nu_2 t)\sigma_z + [gJ_2(\mu)a^\dagger + AJ_0(\mu)]\sigma_- + \text{H.c.} \\ &= \delta a^\dagger a + \frac{1}{2}\varepsilon_2 \cos(\nu_2 t)\sigma_z + \frac{1}{2}B_0\sigma_x + \eta(X\sigma_x - Y\sigma_y), \end{aligned} \quad (\text{S3})$$

where $B_0 = 2AJ_0(\mu)$, $\eta = gJ_2(\mu)/2$, $X = a^\dagger + a$, $Y = i(a^\dagger - a)$, $\sigma_x = \sigma_- + \sigma_-^\dagger$, and $\sigma_y = i\sigma_- - i\sigma_-^\dagger$. Under the unitary transformation $\exp(iB_0\sigma_x t/2)$ and in the limit of $B_0 \gg \eta, \varepsilon_2/2$ and $\nu_2 = B_0$, we obtain the effective Rabi Hamiltonian

$$H_R = \frac{1}{2}\Omega\sigma_z + \delta a^\dagger a + \eta\sigma_x(a^\dagger + a), \quad (\text{S4})$$

where $\Omega = \varepsilon_2/2$ is the effective qubit frequency.

S2. CONTROL OF THE QUENCHING DYNAMICS

A. Time-dependence of the normalized coupling parameter ξ

During the quenching process, we adjust the effective qubit frequency Ω and the effective resonator frequency δ , so that the normalized coupling parameter ξ slowly passes through the quantum transformation critical point:

$$\xi = \lambda/\sqrt{\Omega\delta} = \xi_0 + (\xi_{\max} - \xi_0)t/t_f, \quad (\text{S5})$$

where λ is the qubit-resonator coupling strength, ξ_{\max} (ξ_0) is the maximum (initial) value of $\xi(t)$, and t_f is the total evolution time. For Fig. 1 and Fig. 2 in the main text, we set $\xi_0 = 0.5$, $\xi_{\max} = 2.5$ and $t_f = 3 \mu\text{s}$. Note that, due to the fact practically it's hard to reach the limit of $\Omega/\delta \rightarrow \infty$, we choose and keep $\Omega/\delta = 10$ during the whole quenching process to approximate the preset limitation $\Omega \gg \delta$ of the SPTs. The variances of ξ and Ω over time are plotted and shown in Fig. S1a.

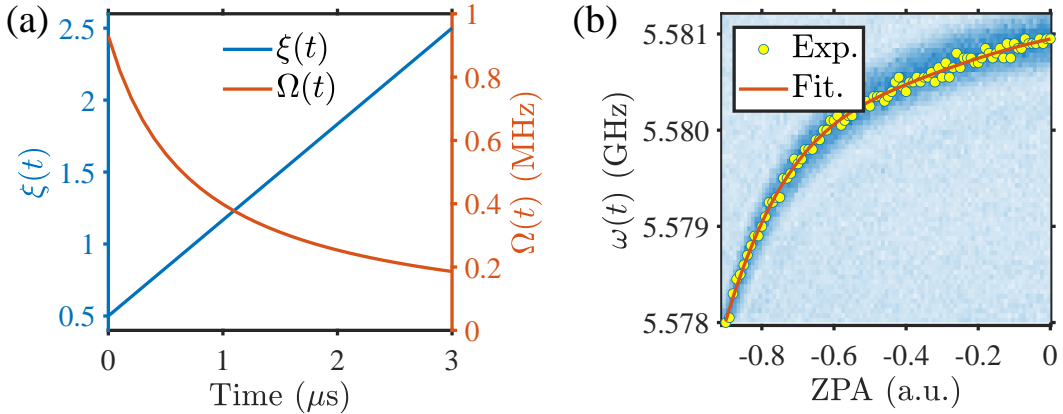


FIG. S1. (a) The normalized coupling parameter ξ and the effective qubit frequency $\Omega(t)$ versus time, exhibiting through the left and right y-axes, respectively. The effective resonator frequency $\delta(t)$ is set as $\Omega/10$. (b) The actual resonator frequency $\omega_r(t)$ versus ZPA. The yellow dots represent the experimental data, with the red solid as a fitting.

B. Control of the effective qubit frequency Ω and the effective resonator frequency δ

According to Eq. (S4), the effective qubit frequency Ω can be constructed by adjusting amplitude ε_2 of the second parametric modulation, with $\Omega = \varepsilon_2/2$. While the effective resonator frequency δ is controllable by tuning the Stark shifts induced by the dispersive coupling of the resonator to an ancilla qubit, whose frequency is flexibly modulable.

When the detuning $\Delta\omega$ between the ancilla qubit and the resonator is varied from $\Delta\omega_1$ to $\Delta\omega_2$, and remains much larger than the coupling strength g' between them, the resulting resonator frequency shift becomes

$$\delta\omega = g' \left(\frac{1}{\Delta\omega_1} - \frac{1}{\Delta\omega_2} \right). \quad (\text{S6})$$

In another form, Eq. (S6) can be written as

$$\delta(t) - \delta(0) = \frac{g'^2}{f(0) - \omega_r} - \frac{g'^2}{f(t) - \omega_r}, \quad (\text{S7})$$

where $g'/2\pi = 20.91$ MHz, and ω_r is the fixed resonator frequency measured with all other qubits staying at their ground states and tuned to their idle frequencies.

For simplicity, to accurately control $\delta(t)$, we directly measure the relationship between the actual resonator frequency $\omega_r(t)$ and the z-line pulse amplitude (ZPA) applied in the ancilla qubit, instead of calculating it from Eq. (S7). We apply a square pulse of a certain amplitude to the Z-line of the ancilla qubit to bias it to the frequency $f(t)$. At the same time, we excite the resonator indirectly by applying a square-envelope with frequency f' to XY-line of the test qubit by crosstalk interactions. Subsequently, we measure the populations of the ancilla qubit after a qubit-resonator swap interaction time π/g' . When the pulse frequency f' is close to $\omega_r(t)$, the resonator will be excited and reflected by the excitation of the ancilla qubit. As shown in the Fig. S1b, the high-value populations show the trend of $f(t)$ and $\omega_r(t)$. At the beginning of the experiment, the ancilla qubit stays at its idle frequency $f_0/2\pi = f(0)/2\pi = 5.93$ GHz, where we define $\delta = \delta(0) = 0$. Therefore the effective resonator frequency $\delta(t)$ can be well controlled.

C. Phase optimization of two longitudinal modulations

To implement the effective Rabi Hamiltonian of Eq. (1) in the main Text, the excitation energy of the test qubit is periodically modulated. However, due to the imperfect waveform of the periodically modulated excitation energy $\omega_q t$, it's necessary to add an optimizable phase to each of the two modulated pulses, in our experiment, of the form

$$\omega_q(t) = \omega_0 + \varepsilon_1 \cos(\nu_1 t + \phi_1) + \varepsilon_2 \cos(\nu_2 t + \phi_2), \quad (\text{S8})$$

so as to validate the most appropriate dynamics of the Rabi Hamiltonian H_R . For simplicity, we assume that ϕ_1 and ϕ_2 are independent of each other. During the dynamic process, ε_2 is slowly decreased. It is fairly assumed herein that the change in ε_2 has no impact on the value of ϕ_2 .

The phase ϕ_1 is optimized first. We apply the first frequency modulation pulse which has a fixed frequency $\nu_1/2\pi = 185$ MHz and amplitude $\varepsilon_1 = 2\pi \times 146$ MHz, and also a transverse microwave drive of an amplitude $A = 2\pi \times 15$ MHz, to the test qubit, initially in $(|g\rangle + |e\rangle)/\sqrt{2}$ state. The effective Hamiltonian is

$$H_{\text{opt}} = gJ_2(\mu)(\sigma^\dagger a + \sigma^- a^\dagger) + AJ_0(\mu)(\sigma^\dagger + \sigma^-). \quad (\text{S9})$$

We traverse ϕ_1 between $-\pi$ and π , and measure the qubit population after 200 ns of the system evolution. By comparing the population oscillation with the ideal numerical simulation results calculated through the evolution under the domination of the Hamiltonian of Eq. (S9), we obtain $\phi_0 = 0$. Before optimizing ϕ_2 , we obtain $\nu_2 = 25.97$ MHz by fitting the population oscillation from the dynamics dominated by Eq. (S9) (with the qubit's $|g\rangle$ state). We iterate over different phases ϕ_2 to carry out the experiments with $\delta = 0$ (by setting the ancilla qubit at its idle frequency) and $\varepsilon_2 = 10$ MHz. Finally, we obtain the one that best coincides with the correspondingly simulated Rabi oscillation curves. Fig. S2a shows the values of the fitting error corresponding to different ϕ_2 . Here the fitting error is defined as $\sum(P_j^g - P_j^{\text{ideal}})^2/N$, where N is the number of data points. Note that we choose the initial state $(|g\rangle - i|e\rangle)/\sqrt{2}$ instead of $|g\rangle$ as previously used because $|g\rangle$ is closer to the eigenstate of the system, and the effect on the population is relatively insignificant. We also slightly adjust the center frequencies and amplitudes of the two modulating pulses in order to improve the control. Based on the previous assumption, we choose the same phase modifications ($\phi_1=0.0$, $\phi_2=-0.45$) for different Ω throughout the experiment.

S3. CHARACTERIZATION OF THE RESONATOR STATE

A. Measurement of photon-number distribution

All the Wigner function values in the main text are deduced from the photon-number distribution of the bus resonator. In the experiment, after a specific time t of the SPTs dynamics evolution, the microwave drive is switched

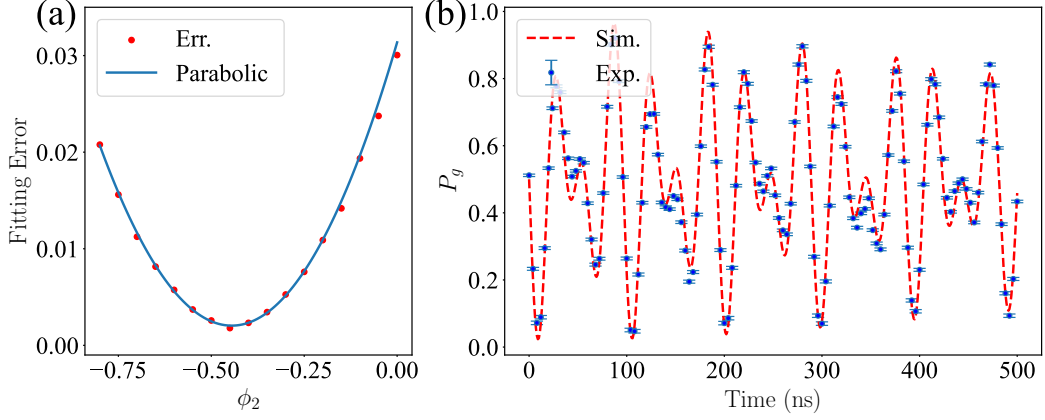


FIG. S2. **Optimizing ϕ_2 and population oscillation.** (a) Fitting errors versus the phase ϕ_2 modification in the experiment. We compare populations with the correspondingly simulated oscillations by calculating the fitting error of the difference of the two populations (dots) and find the best ϕ_2 (x-axis) by locating the minimum of the fitted parabolic (blue solid line). (b) Fitting for $\phi_1 = 0.0$ and $\phi_2 = -0.45$. The populations P_g of the ground state of the test qubit versus time. The blue dots and red dashed line represent the experimental data and the correspondingly numerical fitting results, respectively.

off. A displacement operation is applied to the resonator by a resonant pulse of 100 ns. Then, we bias the ancilla qubit from its idle frequency of 5.93 GHz to the frequency of 5.581 GHz where it is resonantly coupling with the resonator for a given time τ . In this case, the ancilla qubit undergoes photon-number-dependent Rabi oscillations. The populations $P_e^a(\tau)$, of the excited state of the ancilla qubit for a given interaction time τ , are measured by biasing it back to its idle frequency, where the state readout is performed. The quantum Rabi oscillation signals can be fitted as

$$P_e^a(\tau) = \frac{1}{2} \left[1 - P_g^a(0) \sum_{n=0}^{n_{max}} P_n e^{-\kappa_n \tau} \cos(2\sqrt{n}\lambda'\tau) \right], \quad (\text{S10})$$

where P_n denotes the n -photon state distribution probability, n_{max} is the cutoff of the photon number in the fitting program, $P_g^a(0)$ indicates the probability that the ancilla qubit is initially in the ground state, and $\kappa_n = n^l/T_{1,p}$ ($l = 0.7$) [S1–S5] is the empirical decay rate of the Rabi oscillations associated with the n -photon state. It is worth noting that due to the finite detuning $\Delta/2\pi = 0.392$ GHz between the ancilla qubit and the bus resonator, as the number of photons increases, the ancilla qubit inevitably interacts with the resonator during the SPTs dynamics, the ground state population $P_g^a(0)$ may not be 1 at $\tau = 0$. This induces a slight entanglement between the ancilla qubit and the resonator. Referring to [S1], we ignore the small excitation of $|e\rangle$ and $P_g^a(0)$ is introduced to make the fitting more accurate. We then use the least square method to fit the experimental data according to Eq. (S10) to obtain the actual photon number distribution, average photon number $\bar{n} = \langle a^\dagger a \rangle$, and further the Wigner function. Based on the measurements and the fitting operations described above, we can give the evolution of the average photon number in the resonator, as shown in the Fig. S3.

B. Reconstruction of conditional Wigner functions

As described in the main text, the resonator's Wigner function associated with the qubit state $|j\rangle$ ($j = e, g$) is given by

$$\mathcal{W}_j(\beta) = \frac{2}{\pi P_j} \sum (-1)^n P_{j,n}(\beta), \quad (\text{S11})$$

where $P_{j,n}(\beta) = \langle j, n | D(-\beta) \rho D(\beta) | j, n \rangle$, and P_j is the probability of detecting the qubit in $|j\rangle$ -state. The photon number distribution $P_{j,n}(\beta)$ of the displaced field state associated with the state $|j\rangle$ of the test qubit can be extracted by resonantly coupling an ancilla qubit to the resonator, and correlating the observed Rabi signal to the measurement outcome $|j\rangle$ of the test qubit. Here, to fit the photon-number-dependent Rabi oscillations better, we try to select the time point where the test qubit $|g\rangle$ and $|e\rangle$ states' populations are close to each other. With the increase of the photon number and thus also the expanded phase space, the fitting of the photon population becomes inaccurate. Some

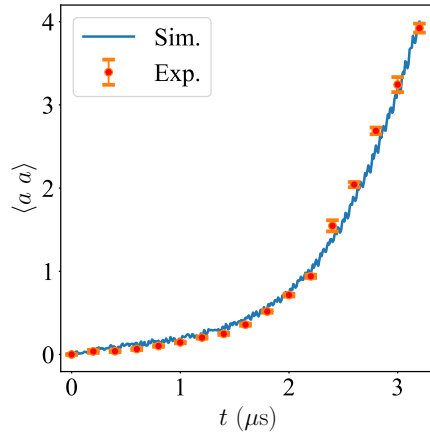


FIG. S3. **Observed dynamical evolution of the average photon number** $\bar{n} = \langle a^\dagger a \rangle$. The red dots represent the average number of photons obtained from the population distribution in the experiment and the corresponding simulation result is shown by the blue curve.

points with large fitting errors are neglected when we reconstruct the density matrix. A group of Wigner functions need to be continuously collected for 20 hours, and it is difficult to maintain qubit performance for a long time, so we again bring up qubits during the data collection process and the related data lacks error bars.

After that, we use the CVX toolbox based on MATLAB [S6] to realize density matrix $\rho_{j,k}$ reconstruction from Wigner functions $\mathcal{W}_{j,k}$. The solved density matrix $\rho_{k,k}$ is Hermitian and positive semidefinite as well as satisfying $\text{Tr}(\rho_{k,k}) = 1$. The raw Wigner data at $t = 2.8 \mu\text{s}$ and the corresponding Wigner functions calculated by the reconstructed density matrix are shown in Fig. S4, respectively. And we take the same treatment as that for Fig. 2 in the main Text.

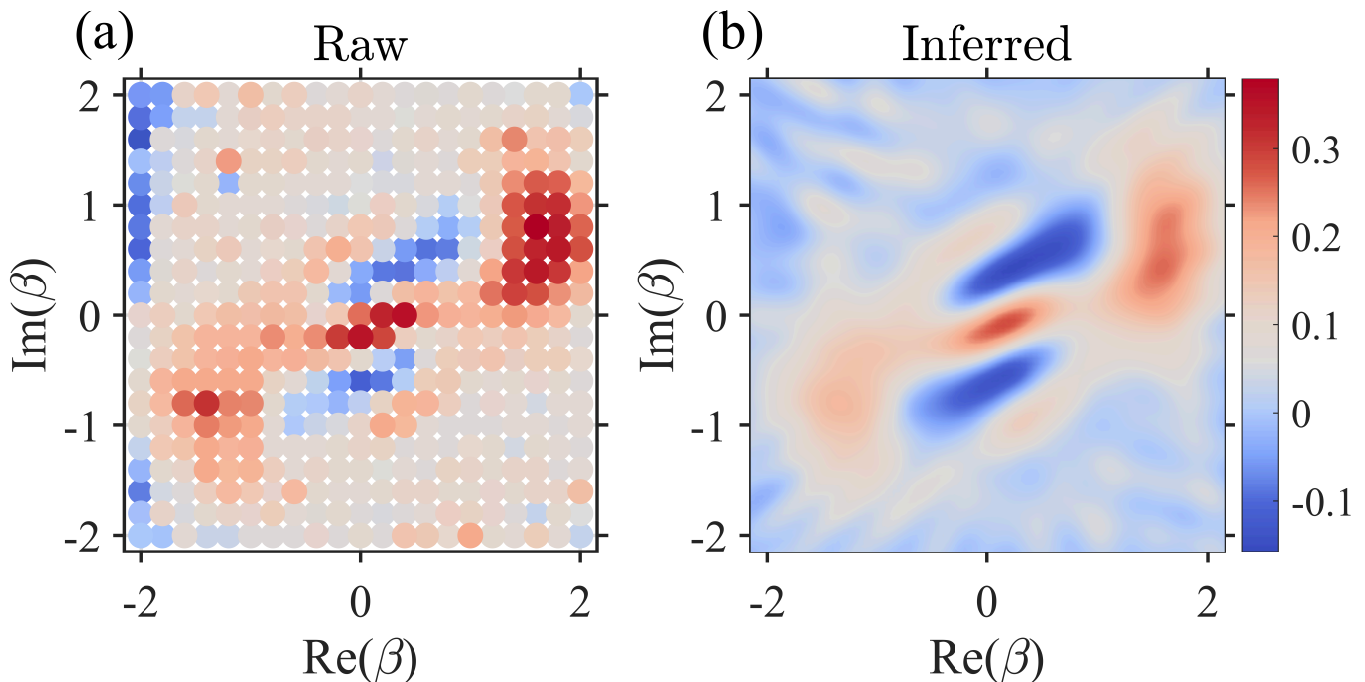


FIG. S4. **Comparison of raw and inferred Wigner functions.** (a), (e), (i) Raw Wigner functions associated with the $|e\rangle$ -state of the test qubit at 2.5, 2.8, and 3.0 μs . (c), (g), (k) Raw Wigner functions associated with the $|g\rangle$ -state of the test qubit at 2.5, 2.8, and 3.0 μs . (b), (d), (f), (h), (j), (l) Correspond inferred Wigner functions deduced from the raw data by CVX.

C. Correction of the phase-space rotations

For a more intuitive description of the phase space, we also use the Q-function to characterize the phase space distribution, defined as, $Q(\gamma) = \frac{1}{\pi} \langle \gamma | \rho_r | \gamma \rangle$, where $|\gamma\rangle$ is the coherent state with a complex amplitude γ and ρ_r is the reduced density operator of the resonator, which is obtained by reconstruction of the corresponding Wigner functions. In the experiment, when the test qubit is in its $|e\rangle$ and $|g\rangle$ states, two factors cause the resonator states to rotate differently. One is due to a slight difference between the experimental frame and the effective Hamiltonian frame, and the other is generated by the resonator's Wigner tomography pulse. Hence, after reconstructing the density matrix ρ_k from the Wigner tomography \mathcal{W}_k , which is the reduced density operator of the resonator when the test qubits in $|k\rangle$ state, we add a rotation operator on the corresponding density matrix numerically. The rotation operator is defined as

$$U_k = \exp[-i\theta_k t/t_f a^\dagger a], \quad (\text{S12})$$

$$\rho'_k = U_k \rho_k U_k^\dagger, \quad (k = e, g) \quad (\text{S13})$$

and ρ_r is obtained by adding two rotated ρ'_k according to the corresponding qubit state population:

$$\rho_r(t) = P_e^t \rho'_e(t) + P_g^t \rho'_g(t). \quad (\text{S14})$$

Here we choose $(\theta_e, \theta_g, t_f) = (10.6, 10.2, 3.0 \mu\text{s})$ in the simulation.

The phase-space coordinates of the phase-space local maxima α_- and α_+ in Fig. 1 in the main text was not well distinguished before $2 \mu\text{s}$, so we performed Gaussian fitting on the data, as shown by the dashed line in Fig. 1b.

S4. NUMERICAL SIMULATION

To further confirm the accuracy of the experimental results, we use the original Hamiltonian Eq. (S1) for numerical simulation for which the qubit's third level is included. We subtract the Stark term of the $a^\dagger a$ form to make the results more accurate, achieved experimentally by slightly adjusting the frequency of the auxiliary qubit. For simplicity, we directly shift the value of δ instead of introducing ancilla qubits, which is reasonable according to Fig. S1b. We plot the population of the third level $|f\rangle$ in Fig. S5, with the results showing that the average population of $|f\rangle$ is about 0.016 during the quenching dynamics, while the maximum population is 0.046. It can be seen that the second excited state $|f\rangle$ has little influence on the evolution of the dynamics of the test qubit.

The simulated average photon number has been shown in Fig. S3, and the corresponding Wigner function of the diagonal elements are shown in Fig. S6. These five columns show the Wigner functions at different times: 1.0, 2.0, 2.5, 2.8, and 3.0 μs .

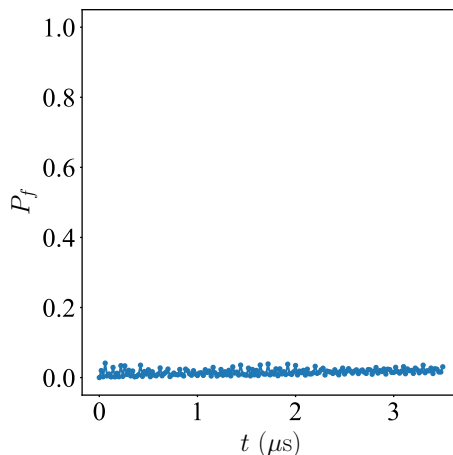


FIG. S5. Numerically simulated population of the third level $|f\rangle$ versus times.

[S1] M. Hofheinz *et al.*, “Synthesizing arbitrary quantum states in a superconducting resonator,” *Nature* **459**, 546–549 (2009).

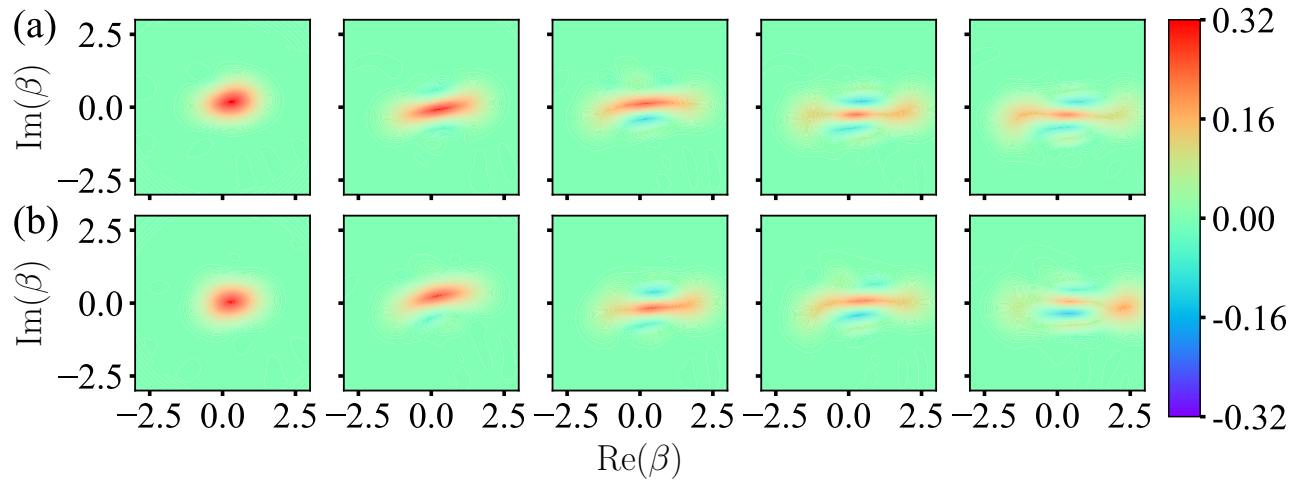


FIG. S6. **Observation of the loss of the quantum coherence in numerical simulation.** (a) Conditional Wigner function $\mathcal{W}_e(\beta)$; (b) $\mathcal{W}_g(\beta)$ measured after quench times $t = 1.0, 2.0, 2.5, 2.8,$ and $3.0 \mu\text{s}$.

- [S2] D. M. Meekhof, C. Monroe, B. E. King, W. M. Itano, D. J. Wineland, “Generation of nonclassical motional states of a trapped atom,” *Phys. Rev. Lett.* **76**, 1796–1799 (1996).
- [S3] D. Leibfried, R. Blatt, C. Monroe, D. Wineland, “Quantum dynamics of single trapped ions,” *Rev. Mod. Phys.* **75**, 281–324 (2003).
- [S4] D. Lv *et al.*, “Quantum simulation of the quantum Rabi model in a trapped ion,” *Phys. Rev. X* **8**, 021027 (2018).
- [S5] M.-L. Cai *et al.*, “Observation of a quantum phase transition in the quantum Rabi model with a single trapped ion,” *Nat. Commun.* **12**, 1126 (2021).
- [S6] M. Grant, S. Boyd, CVX: Matlab software for disciplined convex programming, version 2.0 beta. <http://cvxr.com/cvx>, September (2013).